Transition of Stratus into Fog along the California Coast: Observations and Modeling

DARKO KORAČIN

Desert Research Institute, Reno, Nevada

JOHN LEWIS

National Severe Storms Laboratory, Norman, Oklahoma, and Desert Research Institute, Reno, Nevada

WILLIAM T. THOMPSON

Naval Research Laboratory, Monterey, California

CLIVE E. DORMAN

Scripps Institution of Oceanography, La Jolla, California, and San Diego State University, San Diego, California

JOOST A. BUSINGER

University of Washington, Seattle, Washington

(Manuscript received 6 January 2000, in final form 5 September 2000)

ABSTRACT

A case of fog formation along the California coast is examined with the aid of a one-dimensional, higher-order, turbulence-closure model in conjunction with a set of myriad observations. The event is characterized by persistent along-coast winds in the marine layer, and this pattern justifies a Lagrangian approach to the study. A slab of marine layer air is tracked from the waters near the California–Oregon border to the California bight over a 2-day period. Observations indicate that the marine layer is covered by stratus cloud and comes under the influence of large-scale subsidence and progressively increasing sea surface temperature along the southbound trajectory.

It is hypothesized that cloud-top cooling and large-scale subsidence are paramount to the fog formation process. The one-dimensional model, evaluated with various observations along the Lagrangian path, is used to test the hypothesis. The principal findings of the study are 1) fog forms in response to relatively long preconditioning of the marine layer, 2) radiative cooling at the cloud top is the primary mechanism for cooling and mixing the cloud-topped marine layer, and 3) subsidence acts to strengthen the inversion above the cloud top and forces lowering of the cloud. Although the positive fluxes of sensible and latent heat at the air–sea interface are the factors that govern the onset of fog, sensitivity studies with the one-dimensional model indicate that these sensible and latent heat fluxes are of secondary importance as compared to subsidence and cloud-top cooling. Sensitivity tests also suggest that there is an optimal inversion strength favorable to fog formation and that the moisture conditions above the inversion influence fog evolution.

1. Introduction

Although fog along the California coast is of immediate and practical importance to the marine and aviation communities, a fundamental understanding of the phenomenon remains elusive. It appears that similar synoptic regimes in the eastern Pacific–western United States can lead to fog in one case but not in another. The timescale of the synoptic disturbance and the associated path history of the marine layer air are likely to have bearing on the occurrence of fog. The marine layer is disturbed by the passage of a cyclone/front, and recovery to a state that is conducive to the formation of fog/stratus is dependent on the interplay between large-scale forcing and boundary layer processes. Understanding of this interplay is generally hampered by the scarcity of measurements over the ocean.

Examination of earlier work makes it clear that fog over land has received considerably more attention than fog at sea. Fog over land is categorically divided into advection and radiation types (Duynkerke 1991, 1999). One of the earliest and most notable studies of fog at

Corresponding author address: Dr. Darko Koračin, Desert Research Institute, 2215 Raggio Parkway, Reno, NV 89512.
E-mail: darko@dri.edu

sea was made by G. I. Taylor in the aftermath of the *Titanic* disaster (Taylor 1917; Batchelor 1996). His measurements were made over the Banks of Newfoundland, which is characterized by exceptionally cold water. He found that the water was colder than the air in 80% of the 141 cases of fog he observed. Petterssen (1938) investigated critical parameters for fog formation along the California coast and found that fog also formed over warm waters. He indicated that radiative cooling of the fog layer, together with heating from the sea surface, initiates mixing and lifting of the marine inversion, which consequently influences fog evolution. Pilié et al. (1979) also found that the sea surface was warmer than the air in all of the fog events that they observed off the California coast (30 total events). Although the general rule appears to be that fog events are associated with a warm sea surface, Leipper (1948) and Dorman et al. (1998) documented cases of fog adjoining the California coast where the sea surface was colder than the near-surface air. Leipper (1994) discussed this issue among others in a historical review of West Coast fog.

Anderson (1931) first reported the formation of fog along the California coast by a stratus-lowering process. He studied fog with an instrumented aircraft in the vicinity of San Diego, California, during the summer and fall of 1929. Anderson concluded that fog results from the cloud-lowering process when the initial inversion is sufficiently low—less than 1000 ft—and cloud-top radiation persists.

The mechanism of stratus lowering (thickening) to fog caused mainly by microphysical processes and entrainment has also been investigated by Oliver et al. (1978), Pilie et al. (1979), and Telford and Chai (1984). Some of the other mechanisms that have been identified by Pilie et al. (1979) include fog triggered by instability and mixing over warm water patches and radiation fog formed over the land and then advected to sea by nocturnal land breeze. The relative frequency of fog formation stimulated by the various mechanisms is unknown; however, Filonczuk et al. (1995) carefully documented the meteorological conditions that accompany fog episodes in six geographical regions along the California coast. They found that fog is formed over a wide range of meteorological and sea conditions including wind speed and direction, sea surface temperature, and air–sea temperature difference. The lack of any spatial uniformity in the seasonal distribution of fog is a fundamental result of their climatological study.

The Cornell Aeronautical Laboratories Corporation (Calspan), under contract to the U.S. Navy, made the most complete observational investigation of California coastal fog due to stratus lowering as well as the other mechanisms mentioned above. The results of the Calspan field work are found in a series of technical reports (most notably by Mack et al. 1974) and a summary journal article by Pilié et al. (1979). Oliver et al. (1978) made use of the Calspan field data to model offshore fog. Typical thermodynamic profiles derived from the field measurements were used in conjunction with a one-dimensional boundary layer model to simulate the event.

In our study of California coastal fog due to stratus lowering, we pay particular attention to changes in the marine layer as a result of long overwater trajectories in the presence of large-scale subsidence and a strong low-level inversion. In the early spring study that is the focus of our investigation, we show that the along-coast winds are persistent for several days. This leads us to view the process in a Lagrangian framework, where the marine layer air mass progressively moves from the waters off the northern California border to the California bight (the open bay south of Point Conception). We use a one-dimensional, second-moment, turbulence-closure boundary layer model in the Lagrangian framework to study the fog formation process. Results from the simulation are compared to meteorological data at various points along the trajectory. Through use of a simulated evolution of offshore fog in conjunction with the observations, we intend to clarify the interplay of cloud-top cooling, strong subsidence, and low-level inversion on the evolution of fog and to determine the importance of these mechanisms.

2. Synthesis of observations related to April 1999 fog event

The fog event took place in mid-April 1999. When we reference the day and time within the time period, we will omit the year. Also, as a point of reference, 1200 UTC is equivalent to 0400 LST in California.

Regarding the designation of observed fog, we adhere to the definitions of visibility set forth in *Meteorology for Mariners* (British Meteorological Office 1978, chapter 5). Thus, atmospheric visibility reduced to less than 1 km is classified as heavy fog (dense) and visibility greater than 1 km is classified as light fog (synonymous with mist). Figure 1 shows the location of various geographical landmarks and other points important to this study.

a. Large-scale subsidence

The stratus–fog event occurred in conjunction with a synoptic disturbance that moved into the West Coast on 11 April 1999. The cyclone moved rapidly through the region, and the trailing anticyclone entered the northwestern United States at 1200 UTC 13 April. This anticyclone progressively moved from the Northwest through the Great Basin and southwestern United States during a period of several days and effectively blocked the entry of other cyclones into the West Coast.

The general character of the flow associated with the anticyclone is depicted by the streamlines along the 300 K isentropic surface shown in Fig. 2. In the figure, we note a wide sweep of northeasterly flow emanating from the high-pressure center just north of Quillayute, Washington. As this air moves toward the coast, it descends

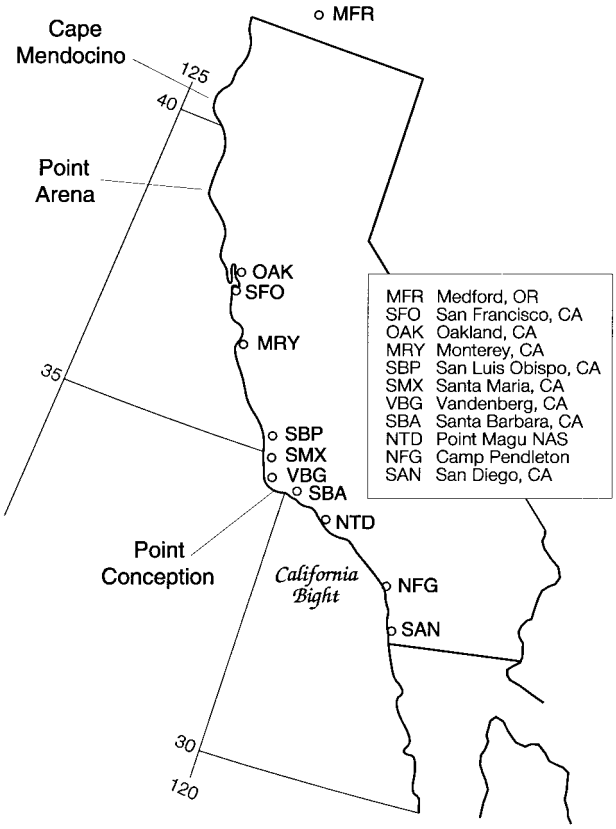

FIG. 1. Map of various geographical locations and positions of surface and upper-air stations referenced in this study.

at rates ranging from 1 to 3 cm s^{-1}, with the maximum occurring over central California. These rates of descent are faster than those reported by Neiburger et al. (1961) in their climatological study of stratus along the California coast in summertime. Examination of their Fig. 39 indicates that vertical velocities of ≈ -1 cm s^{-1} are the extremes at 700 mb. Considering the strength of the anticyclone under investigation compared to the climatological situation in summer, the faster descent rates seem reasonable.

Along the central California coast, the 300 K surface is approximately 900 m above sea level. This is 300–500 m above the marine inversions shown in Fig. 3. Between 1200 UTC 13 April and 1200 UTC 14 April, the marine inversion descended from ≈600 m to ≈200 m at Oakland, California (OAK). The estimated height of the inversion at 1200 UTC 14 April is based on the moisture profile. The rate of descent is generally governed by large-scale subsidence in combination with boundary layer processes that tend to offset inversion height descent. These issues will be discussed further in the modeling section.

While the airflow just above the marine layer is directed from land to sea and is essentially perpendicular to the California coastline, the winds in the marine layer are northwesterly and tend to parallel the coast. Figure 4 shows the 48-h trajectory of the surface marine layer air that is tracked backward from Santa Barbara, California. Trajectory calculation followed the methodology outlined by Saucier (1955).

b. Evolution of clouds and fog

Stratus cloud was scattered over the coastal waters from Cape Mendocino to central California on the morning of 12 April (≈1600 UTC). By the morning of 13 April (≈1600 UTC), the skies along the coast were completely covered with stratus (Fig. 5). We determined the percentage of sky coverage and cloud type using processed *GOES-10* data supplied by the Space Science and Engineering Center at the University of Wisconsin—Madison (R. Rabin 2000, personal communication). The cloud layers gradually moved southward, and coastal stations north of Point Conception were cloud free by 1600 UTC 15 April.

Fog was first detected between Monterey and Vandenberg Air Force Base (AFB), California, at 0300 UTC 14 April. As shown in the time series plot in Fig. 6, the low-visibility conditions and fog generally moved southward and reached San Diego by 0600 UTC 15 April. The stations near Point Conception (SBP, SMX, and VBG) exhibited foggy conditions during the night and early morning hours (≈0600–1500 UTC), whereas stations along the coast of the California bight (SBA, NTD, and SAN) exhibited fog in the afternoon hours as well as at night and in the early morning. The variability of wind direction in both space and time at these coastal stations is in marked contrast to the constancy of wind direction offshore.

c. Trends at the air–sea interface

In Fig. 7, we display temperature, dewpoint temperature (where available), and the sea surface temperature (SST) trends during a 2-day period. From Eel River (north) to Port Arguello (south), we note that SST increases by ≈2 K. It is also apparent that the air–sea temperature differences are relatively small north of San Francisco, California, but are on the order of 1–2 K at San Francisco and points south on 13–14 April. Most notable is the approach to saturation of the near-surface air at Port Arguello between 0000 and 1200 UTC 14 April.

3. Conceptual modeling of processes leading to fog formation—Lagrangian approach

The foregoing data analysis indicates that offshore fog forms as a result of modification of the cloudy marine layer as it tracks over extended stretches of coastal water. The modification occurs in conjunction with large-scale subsidence and increasing SST along the path. In order to understand the modification of the

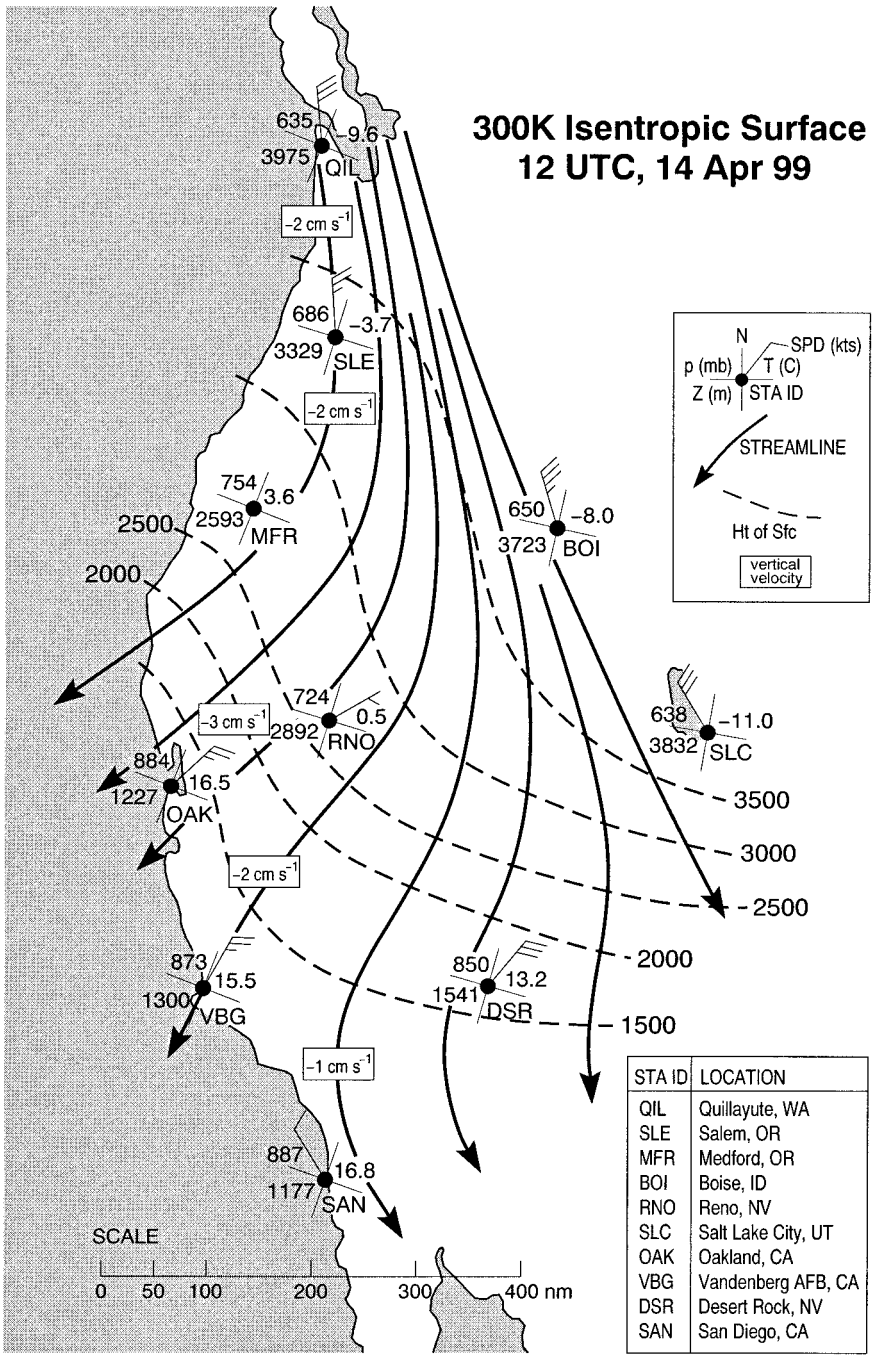

FIG. 2. Analysis of the 300 K isentropic surface based on upper-air data from the western United States.

cloudy marine layer, we designed a numerical experiment that simulates this process and utilizes satellite, buoy, and radiosonde data to evaluate the results. Central to the experiment is a one-dimensional, higher-order, turbulence-closure model. We use this model with high vertical resolution to simulate a 2-day evolution of the cloudy marine layer and to test the hypothesis that radiative cooling and subsidence are crucial to fog formation.

Although one-dimensional models do not account for advective processes, they permit a measure of completeness in studies of sensitivity that is impossible with three-dimensional models. Furthermore, it is often possible with the use of one-dimensional models to unravel

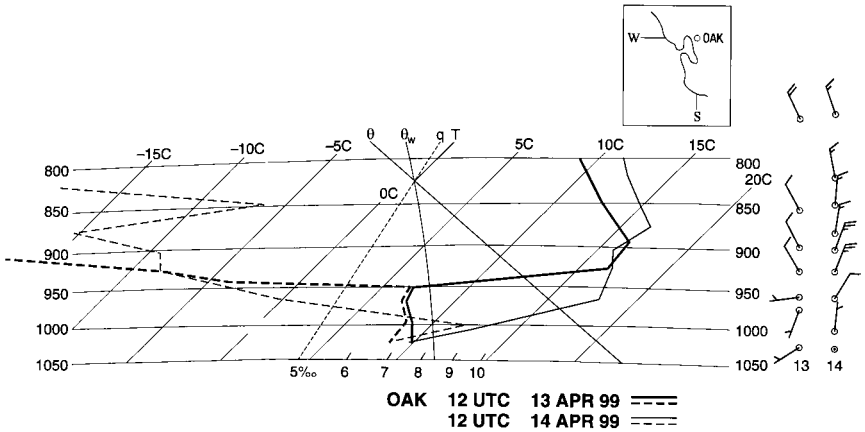

FIG. 3. Plot of upper-air soundings taken at Oakland at 1200 UTC 13–14 Apr 1999. Solid lines are temperature, and dashed lines are dewpoint temperature. Data are plotted on a tephigram where the orientation of the various isolines is depicted in the top-central area of the figure. The variables are wet-bulb potential temperature (θ_w), potential temperature (θ), water vapor mixing ratio (q), and temperature (T). The pressure levels from 1050 to 800 mb are indicated on both sides of the diagram. Winds (in knots) are shown on the right side of the chart.

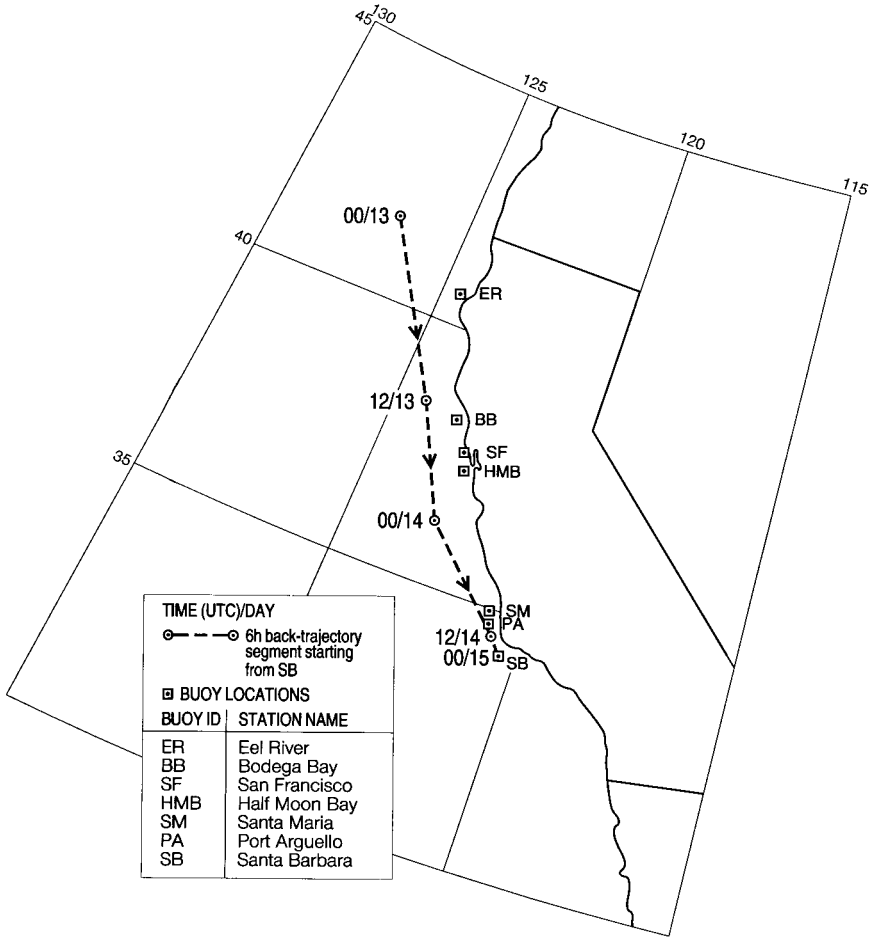

FIG. 4. Backtrajectory of the surface marine layer air during the 2-day period.

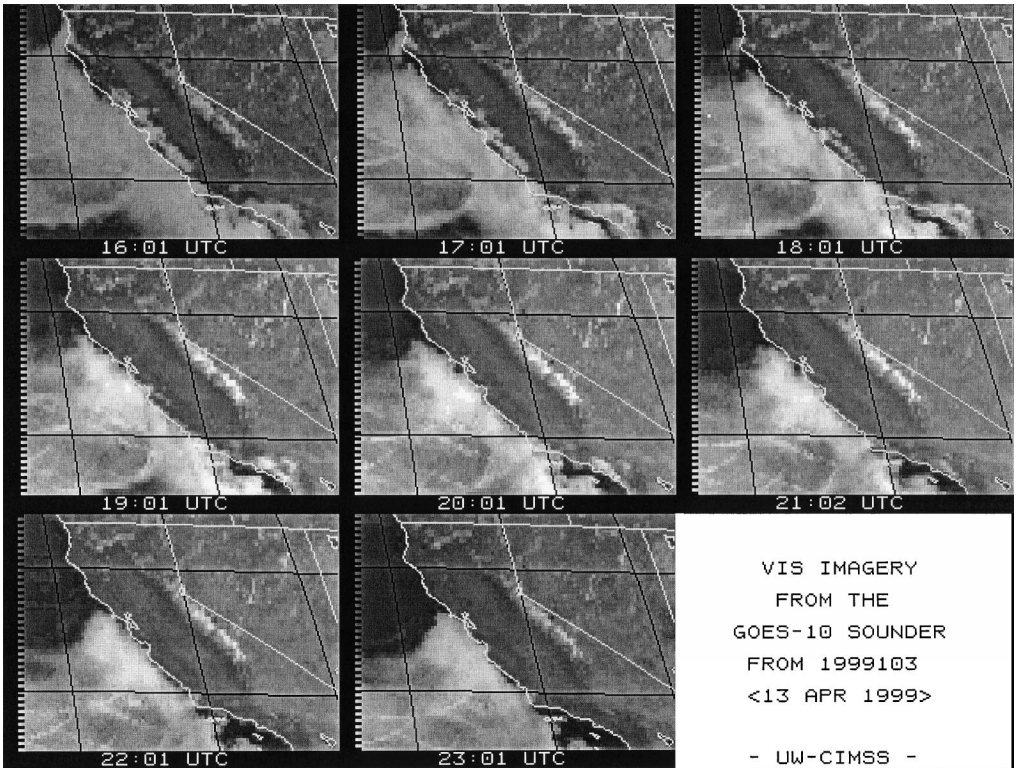

FIG. 5. Visible images of the stratus clouds along the California coast on 13 Apr 1999, taken from the *GOES-10* weather satellite (subsatellite longitude of 135°W). Latitude lines are 35° and 40°N; longitude lines are 115°, 120°, and 125°W.

the complex interactions germane to the occurrence and evolution of phenomena such as offshore fog. This conceptual approach has been used in past studies of the evolution of the atmospheric boundary layer. Examples include 1) use of a one-dimensional mixed-layer model to study changes in temperature and humidity of the atmospheric layer as the air crossed Lake Ontario (Stage and Businger 1981a,b), 2) application of the model used in this study to investigate the response of the cloudy marine atmospheric layer to changes in SST (Koračin and Rogers 1990), and 3) simulation of the evolution of Arctic stratus cloud as it is advected over the Beaufort Sea (Smith and Kao 1996).

The primary justification for our use of a one-dimensional model rests on the presence of persistent along-shore wind. The trajectory shown in Fig. 4 reflects these persistent winds. In the same figure, note that the line connecting the various buoy sites is a reasonable substitute for the actual trajectory during the time period 0600 UTC 13 April–0000 UTC 15 April (a 42-h period). The average horizontal speed along these trajectories is 7–8 m s^{-1}. The model simulates flow along the line of buoy stations during a 48-h period. The simulation represents the advection of a cloud-topped slab of marine layer air as it moves steadily along the coast of California while experiencing forcing from large-scale subsidence, warming from the ocean, and cloud-top radiative cooling.

a. Model

The parameterization used in the present model is based on a one-dimensional version of the three-dimensional, second-order, turbulence-closure mesoscale boundary layer model developed by Yamada (1978). The present model consists of prognostic equations for horizontal wind components, liquid water potential temperature, mixing ratio of total water, and the turbulence kinetic energy. Details of the model structure and its application to radiation and turbulent processes in the cloudy marine atmospheric boundary layer (MABL) are discussed by Koračin (1989), Koračin and Rogers (1990), Rogers and Koračin (1992), and Leipper and Koračin (1998) (see appendix). Turbulent fluxes are calculated from the diagnostic system of second-moment equations. The model includes cloud parameterization and parameterization of longwave and shortwave radiative heat transfer for clear-sky and cloudy conditions. In order to capture the interplay between the cloud–radiative heat transfer effects and turbulent transfer, a grid of 180 vertical points within the 1200-m-deep do-

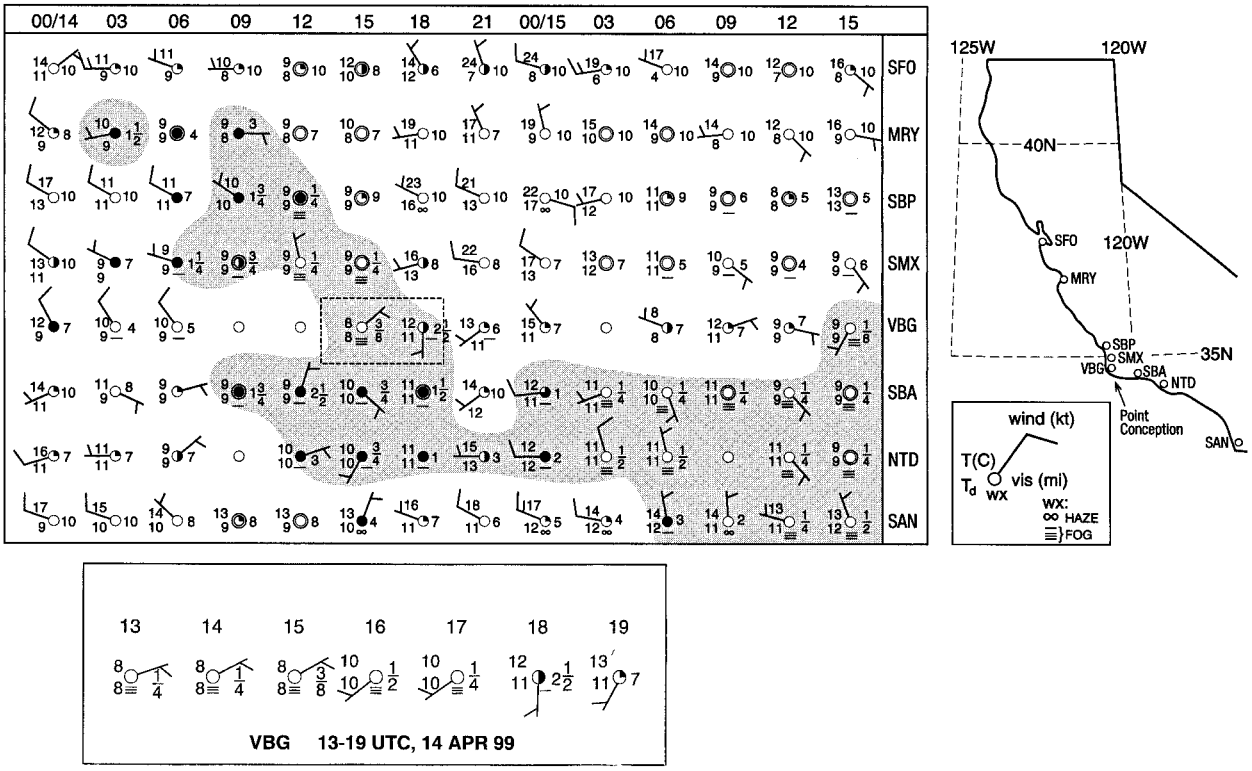

FIG. 6. Time series of weather reports from the airways network along the California coast (3-h intervals). Hourly surface reports from Vandenberg AFB between 1300 and 1900 UTC 14 Apr are displayed on the inset. Shading indicates stations (and times) where visibility is less than or equal to 3 mi.

main is used with the highest resolution of 2 m at the lower boundary.

b. Model setup for a Lagrangian simulation

For the Lagrangian experiment, we consider a slab of the marine atmospheric boundary layer originating at the Eel River buoy site (ER in Fig. 4). By varying SST in time, the model emulates advection of the marine layer slab over increasing SST along the trajectory discussed above. We used Eel River buoy data at 0600 UTC 13 April to establish the initial conditions for the simulation. Initial SST at the Eel River buoy was 9.6°C and SST steadily increased along the trajectory. Based on the initial SST and the SST values at the southern end of the trajectory, we assume a linear increase of 2.0°C (48 h)$^{-1}$ in the simulations. For initial air temperature, we assume an adiabatic profile based on the Eel River temperature of 9.4°C at 3 m. With a pressure of 1023 mb at Eel River, this corresponds to a potential temperature of 7.6°C. Neutral conditions with this potential temperature are assumed within the 600 m deep MABL. An assumed constant water vapor mixing ratio of 6.5 g kg^{-1} produces a cloud layer between the 200- and 600-m levels. The 6.5 g kg^{-1} mixing ratio is based on data from Cape Arago, a coastal marine automated network (C-MAN) station just north of Cape Mendocino.

Geostrophic wind speed of 8 m s^{-1} is assumed in the simulations. Since the advection of the marine layer slab is fundamentally represented by change in SST, this particular value of wind speed is not essential to the model simulation. The crucial element for the simulation is the temporal variation in SST at the lower boundary. We use the Oakland radiosonde data to specify the strength of the marine inversion. According to the soundings at 1200 UTC 13 April and 1200 UTC 14 April, a strong low-level inversion of 10 K was observed at the coast (see Fig. 3); an inversion of this strength between 600 and 700 m was used in the simulation.

The 300 K isentropic analysis indicates subsidence of -3 cm s^{-1} along the central California coast. In the vicinity of Oakland at 1200 UTC 14 April, subsidence velocities as high as -5 cm s^{-1} can be inferred. In further support of subsidence, the Oakland radiosonde data exhibit a lowering of the inversion base by 440 m in 24 h. According to cloud-top temperature estimates from *GOES-10* (R. Rabin 2000, personal communication), lowering of the cloud top (and inversion base by inference) is even greater along the central California coast, with a change of -1047 m in only 15 h. Thus, low-level subsidence in the range of -2 to -5 cm s^{-1}

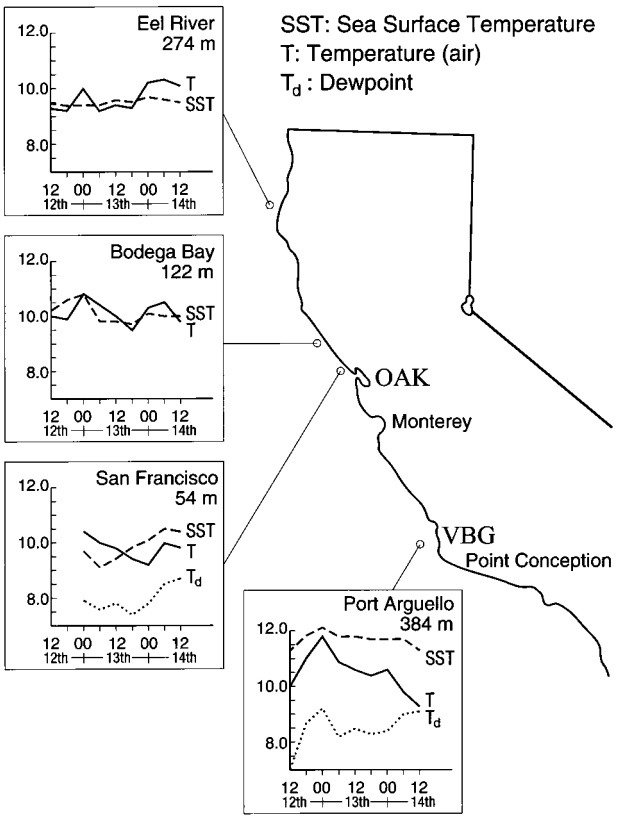

FIG. 7. Buoy data from various sites along the California coast. Ocean depth is indicated in the upper right-hand corner of the plots.

appears to be justified for this case. We performed initial tests with a range of synoptic divergence values that are consistent with a significant lowering of the cloud top in the presence of turbulence. A linear profile of subsidence velocity starting from zero at the surface is assumed in all our simulations. For the baseline run, we assume a constant synoptic divergence of 3×10^{-5} s^{-1} within the model range of 1200 m (equivalent to -3 cm s^{-1} at 1000 m). This divergence value is representative of the synoptic scale, but the actual value could be larger if mesoscale structure is considered. For example, in their study of airflow over Lake Ontario, Stage and Businger (1981a) showed a significant time variation of divergence with values as large as 15×10^{-5} s^{-1}.

c. Simulated and observed transformation of air mass along the trajectory

Data from the line of buoys were compared to the model results. Figure 8 shows the time series of SST, air temperature, and dewpoint temperature at 10 m according to model results and buoy measurements at 5–10 m, respectively. The traces from the line of buoys were found by assuming the surface air moved at a constant rate of 7 m s^{-} between Eel River and Santa Barbara. Field tests with the National Data Buoy Center instruments indicate that air temperature data have an error of ± 0.1°C and dewpoint temperature has an error of ± 0.25°C (D. Gilhousen 2000, personal communication; Breaker et al. 1998). The model shows that the gradual increase in air and dewpoint temperatures is initiated by an increase in SST. Gradual cooling of the near-surface air started after 15 h when the cloud-top cooling became apparent in this layer. The abrupt drop in temperature at 40 h after the initial time in combination with the gradual rise in dewpoint temperature leads to saturation and fog. Observations from the buoys indicate that saturation occurs after 37 h.

The intensity of cloud-top cooling depends on cloud properties as well as the properties of the inversion and the air above the inversion. This will be discussed in the next section. During daytime, this cooling is partially offset by cloud warming associated with solar heating (e.g., Nicholls 1984; Rogers and Koračin 1992). In some cases, solar heating of the cloud can dominate the surface-driven heating of the subcloud layer and lead to stable stratification with a relatively weak thermal inversion at the cloud base. In these cases, cloud-generated turbulence can be decoupled partially or fully from the surface-driven turbulence in the subcloud layer (e.g., Nicholls 1984; Koračin and Rogers 1990; Tjernström and Koračin 1995). Although less intense turbulence could lead to a delay in fog formation, the cumulative amount of cloud-top cooling available for the marine layer will be the same.

The downward propagation of cloud cooling can be seen clearly in the time–height cross section of air temperature (Fig. 9). The onset of cooling first occurs at higher elevations and gradually descends to lower levels. For example, the net cooling begins after 12 h of simulation at 200 m, while it takes 2 more hours for the cooling to reach the 100-m level. Significant cooling occurred after 39 h when the elevated air driven by cloud-top cooling merged with the near-surface layer. The surface airflow trajectory reconstructed from the time series of buoy data shows the same trend: increasing near-surface temperature and dewpoint temperature, at approximately the same rate, as well as a significant drop in these parameters when fog occurred. Note that the actual SST change along the trajectory has strong variations, while in the simulations we assume a simple linear increase in SST. Consequently, the observed near-surface temperature exhibited stronger variations than the modeled one. After the temperature minimum, the near-surface layer is heated by the enhanced positive heat flux associated with increasing SST.

In order to study processes at the air–sea interface and to provide a comparison between model results and observational data, we calculate the bulk-aerodynamic sensible heat flux (HF) and latent heat flux (LF) following Kondo (1975):

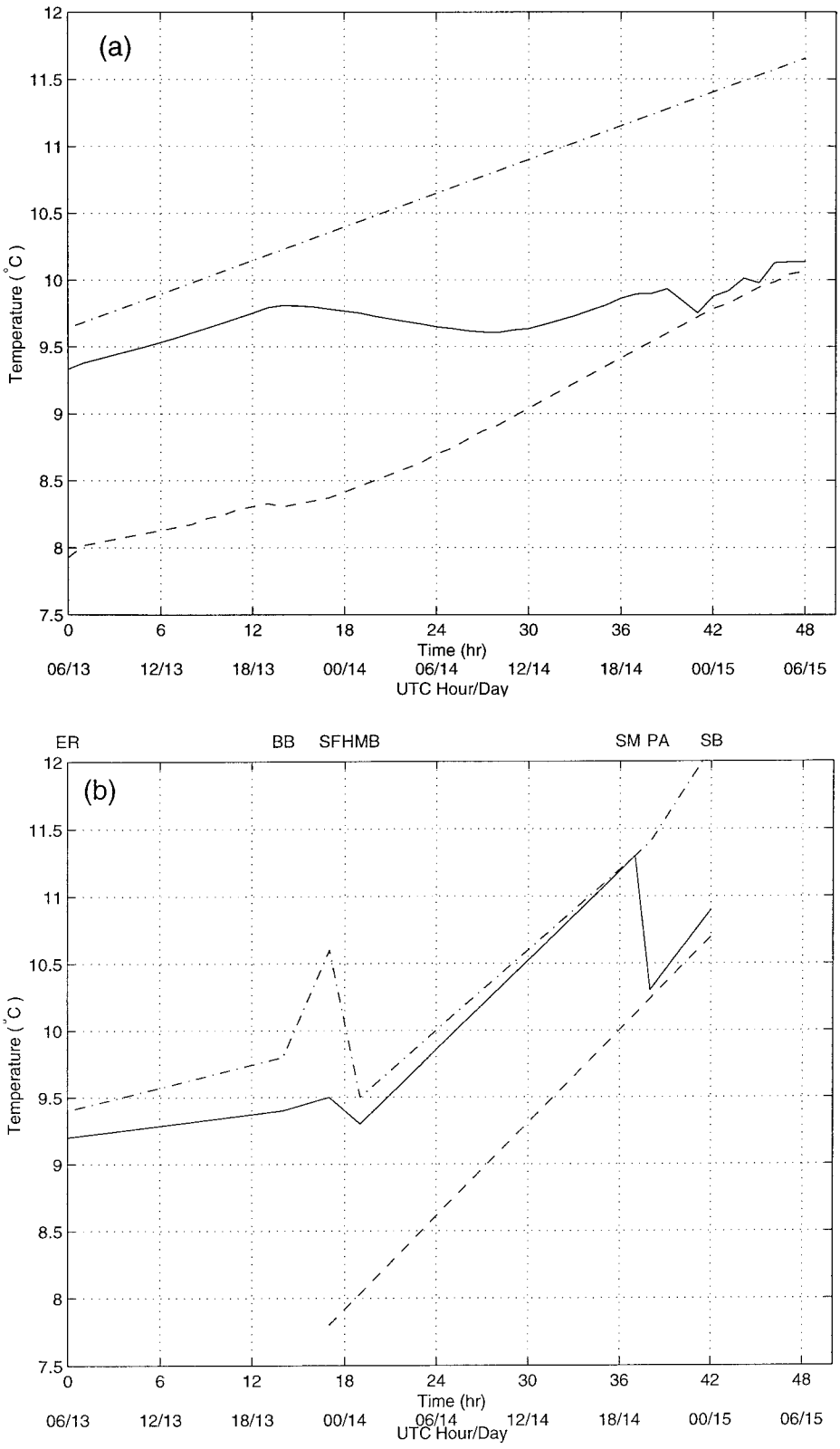

FIG. 8. Time series of near-surface ambient temperature (solid line), dewpoint temperature (dashed line), and sea surface temperature (dash–dotted line), from the model simulation (a) and from the line of buoys shown in Fig. 4 (b) along the trajectory. Buoy locations are indicated along the top horizontal axis.

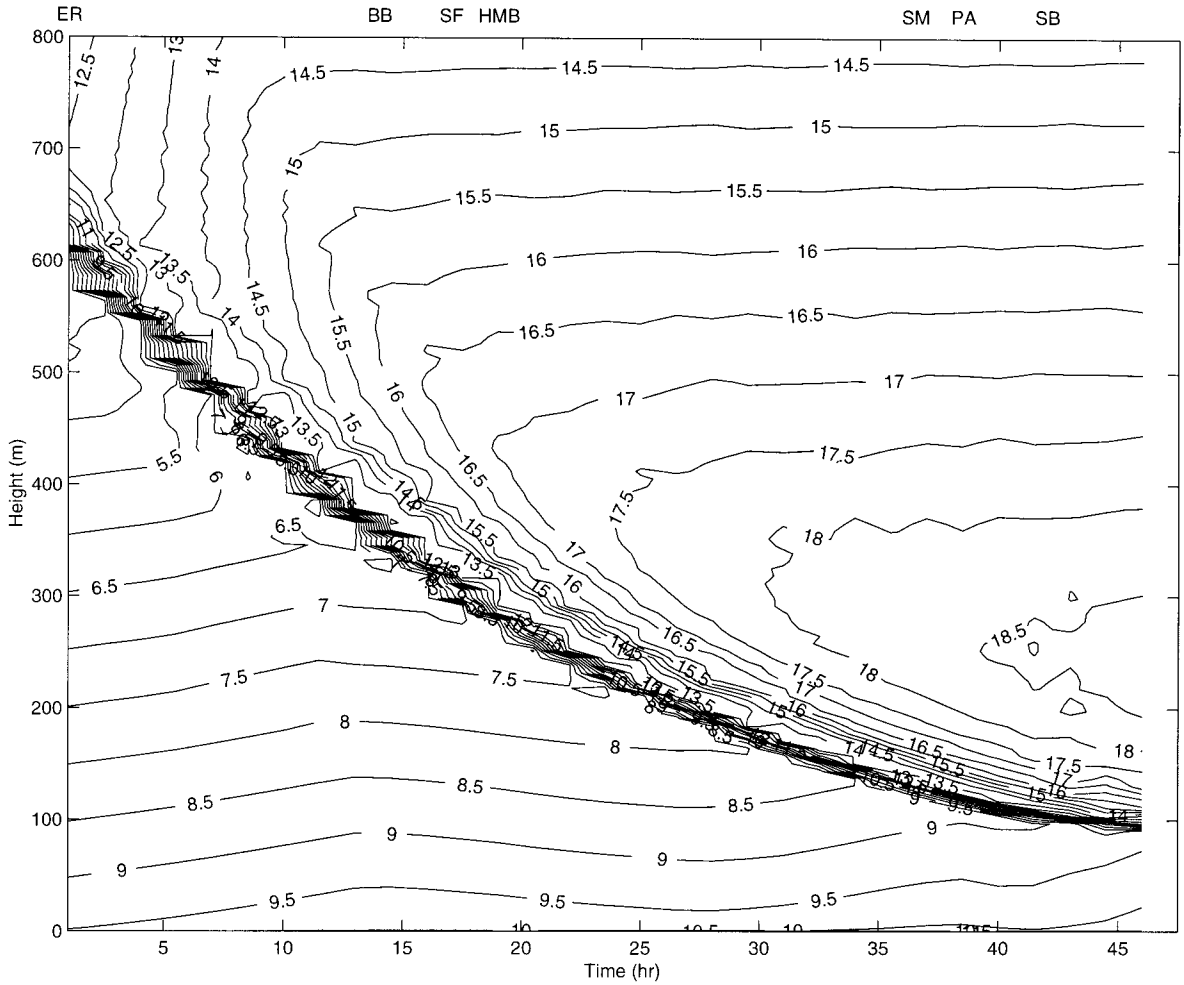

FIG. 9. Contours of ambient temperature (°C) for the baseline simulation. Contour interval is 0.5°C.

$$\mathrm{HF} = \rho c_p c_H (T_s - T_a)|\mathbf{V}|$$

$$\mathrm{LF} = \rho L c_L (q_{vs} - q_{va})|\mathbf{V}|,$$

where the terms of the equations are as follows: ρ, density of air; c_p, specific heat of air at constant pressure; L, latent heat of evaporation; c_H, transfer coefficient for heat; c_L, transfer coefficient for water vapor; T_s, sea surface temperature; q_{vs}, water vapor mixing ratio at sea surface; T_a, air temperature at anemometer height; q_{va}, water vapor mixing ratio at anemometer height; and $|\mathbf{V}|$, wind speed at the anemometer height.

The calculation of turbulent fluxes by these formulae assumes that the upper-level wind speed, air temperature, and mixing ratio are measured at the anemometer height (deck height), nominally 10 m. Since the meteorological data from the buoys are collected at 5–10 m, we introduce an error into these calculations when we use unadjusted data. Based on typical profiles of wind, air temperature, and water vapor mixing ratio, however, we estimate that associated error in the fluxes is less than 10%. Calculations from the model use data at the surface and the 10-m level.

Figure 10 shows these turbulent fluxes calculated from the simulations and the buoy data. Due to an uncertainty of matching an exact location of the air parcel along the trajectory with the buoy location, we averaged the buoy flux for ±3 h around the first-guess corresponding point. The simulated range of sensible and latent heat fluxes (as calculated from the indicated bulk formulas) are in general agreement with observations, but there are some obvious discrepancies in the trends. The applicability of the bulk formulation comes into question when the vapor and temperature gradients are very small in combination with low wind speeds. This is certainly the case near the time of fog formation. Nevertheless, when we calculate the changes in dewpoint temperature based on the flux of 10 W m^{-2} and assume uniform mixing in the lowest 200 m during the last 24 h of the trajectory, we find that this leads to an increase in the dewpoint of approximately 4°C, close to

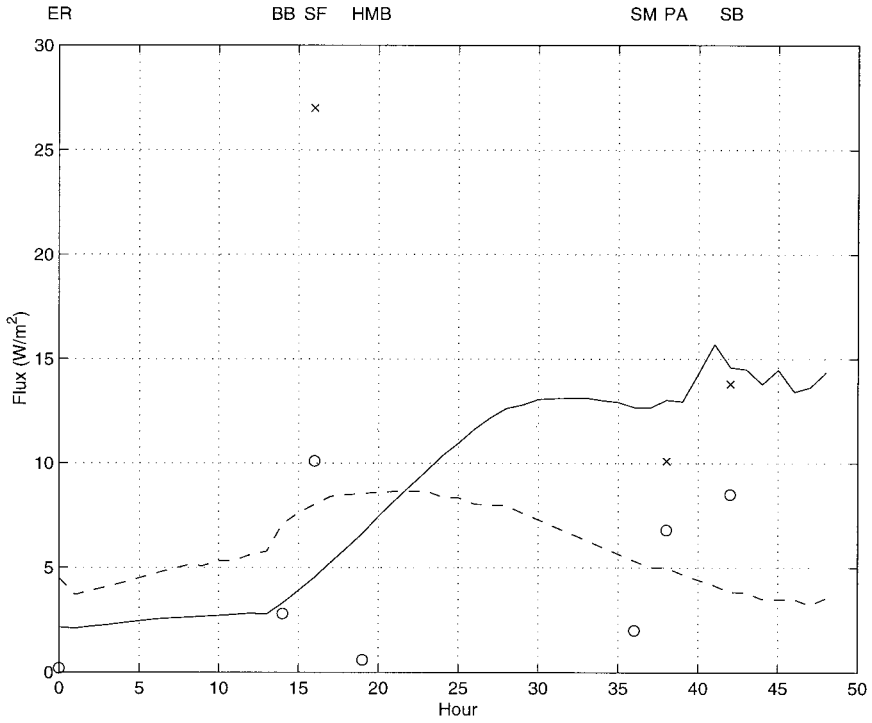

FIG. 10. Time series of the simulated surface sensible heat flux (solid line) and latent heat flux (dashed line) for a baseline simulation with corresponding calculated sensible heat (o) and latent heat (x) fluxes from the buoy data. Buoy locations are indicated along the top horizontal axis.

the observed change. Generally, small positive heat fluxes lead to increases in near-surface temperature and dewpoint temperature, while the cloud-top longwave cooling (Fig. 11) generates cooling in the upper part and gradually throughout the entire marine layer.

Associated evolution of the cloud layer is shown in Fig. 12 through a time series of the simulated cloud base and top. Due to the imposed vertical subsidence profile, the lowering of the cloud top is greater during the first day. The cloud top dropped by approximately 370 m during the first 24 h. Significant lowering of the cloud top and shrinking of the marine layer are confirmed by the radiosonde and satellite data also shown in Fig. 12. Radiosonde estimates of the inversion base at 1200 UTC 13 April and 1200 UTC 14 April are plotted along the Lagrangian trajectory. The rate of decrease of this inversion base exhibits a slope similar to that seen in the model results. Estimates of cloud-top temperature (and associated cloud-top heights) from satellite data suggest an even stronger drop of the cloud top, indicative of strong subsidence and relatively weak marine layer turbulence.

Positive heat flux increased after the near-surface layer started to mix with the cool cloudy air. The increased heat flux partially compensated for the cooling from the cloud top during the second day. When the cloud approaches the near-surface layer, surface fluxes, which increase in response to the warmer sea, reduce the lowering of the cloud. Continuously generated cooling confined in a very shallow boundary layer, however, overcomes surface heating, extends the condensation to the entire marine layer, and produces fog.

d. Sensitivity analysis

We performed a series of sensitivity tests to investigate the importance of subsidence, cloud depth and cloud-top elevation, and moisture properties above the inversion. Here we discuss the primary results.

With an inversion strength of 5 K, warmer and drier air from above the inversion is entrained and results in a rise of the lifted condensation level; however, at the same time, longwave cooling is more intense compared to the baseline simulation and produces increased liquid water content. Figure 13 shows maximum longwave cooling at the cloud/fog top for every hour (extended to 4 days) of the baseline run and for cases with weak and strong inversion. For the weak inversion case, the cloud lowered into the surface layer at a later time (49 h into the simulation) and remained until the end of the test simulation (4 days). Tests with inversion strength of 15 K yielded results similar to the baseline simulation (where the inversion strength was 10 K). In the case of extreme inversion strength (20 K), fog formed 5 h earlier than in the control run but lasted only 10 h. It appears that the strong inversion allowed subsidence to continuously shrink the marine layer and impose strong thermal stability and negative buoyancy at the end of the

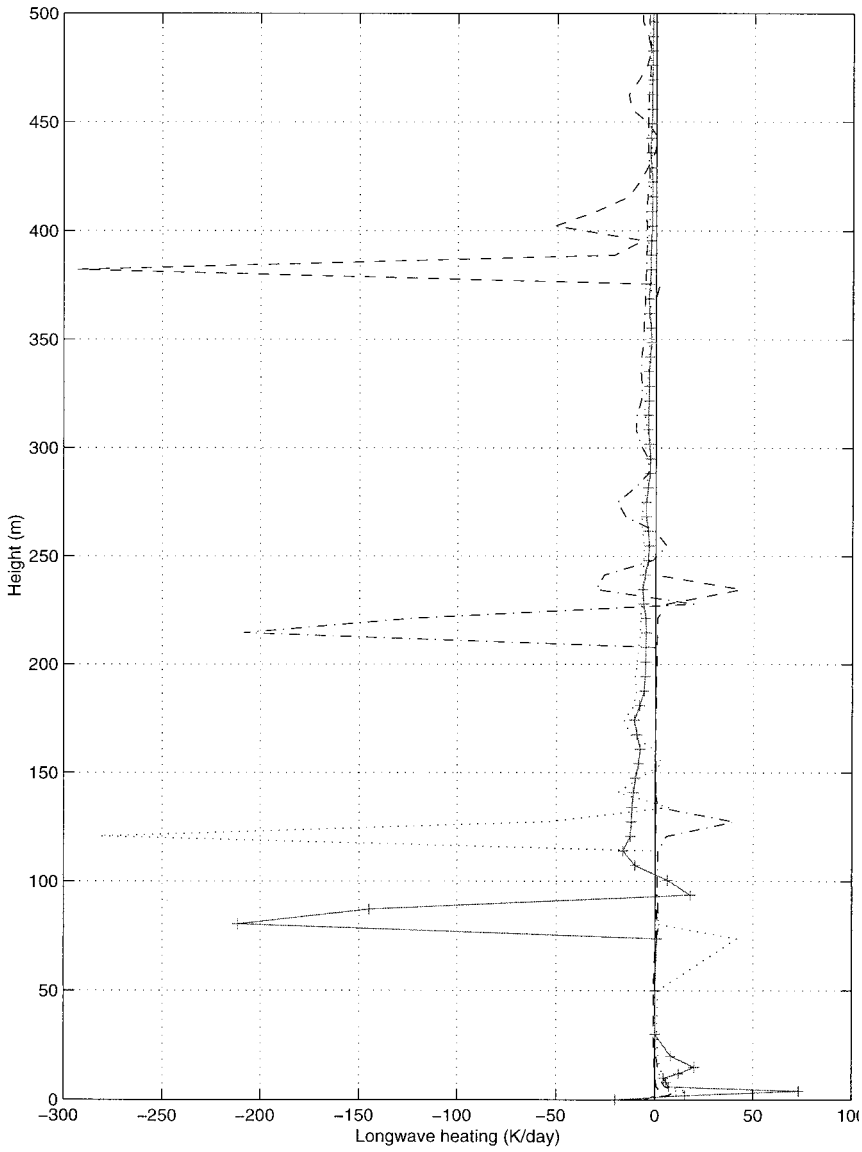

FIG. 11. Vertical profiles of longwave heating (K day^{-1}) at 12 (dashed line), 24 (dash–dotted line), 36 (dotted line), and 48 (solid line) h into the baseline simulation.

simulation (Fig. 14). Less cooling and consequently less liquid water is produced in this case. Radiative thermal heating from the inversion also can contribute to the dissipation of fog within the shallow marine layer (Fig. 11). It appears that optimum inversion strength is in the range of 10 to 15 K, and weaker or stronger inversions can contribute to fog dissipation in our case study.

Subsidence appears to be an important element in determining the formation of fog. A test run with weaker subsidence (divergence of 2×10^{-5} s^{-1}) led to much later fog formation (62 h into the simulation) compared to the baseline run (40 h into the simulation). Stronger subsidence, corresponding to a divergence of 4×10^{-5} s^{-1}, produced fog after only 32 h. In all of these cases, fog was simulated when the cloud top was lowered to a height of approximately 100 m. Note that the cloud drop in the first day of simulation was approximately 280, 370, and 420 m for the ''weak'' subsidence, control run, and ''strong'' subsidence cases, respectively.

A higher initial cloud top of 700 m, but with the same 200-m cloud base used in the control run, yielded transitional cloud lowering at the end of the simulation. The cloud layer was thinner than in the control run, possibly due to the longer time needed for propagation of cloud-top cooling, which consequently allowed the surface heat flux to raise the lifted condensation level. A lower initial cloud top of 300 m led to more rapid cloud lowering to the surface layer (24 h into the simulation) than in the control run (40 h into the simulation). Transitions between fog and stratus are present; that is, the stratus

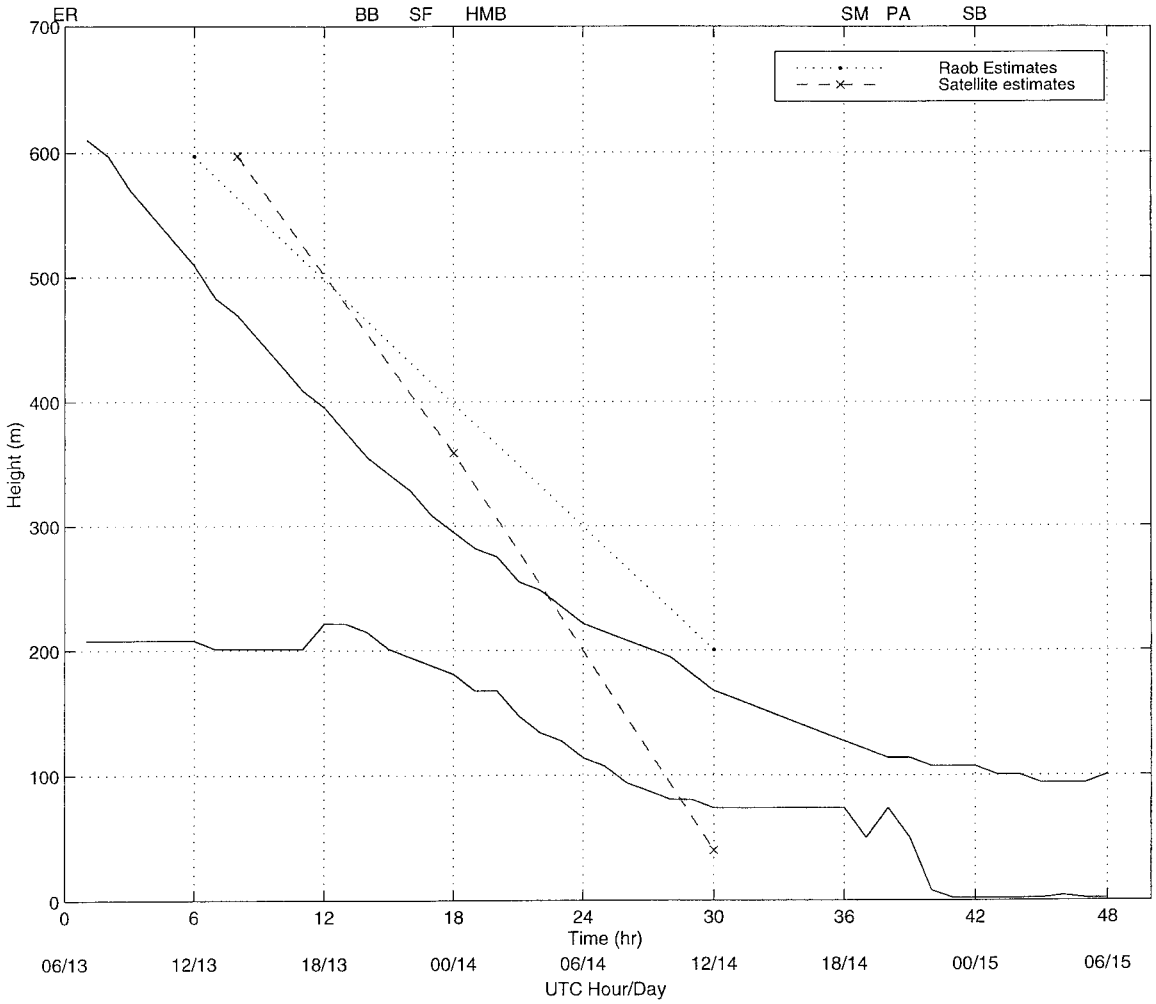

FIG. 12. Time series of the simulated cloud top and base (solid lines) for baseline simulations. An estimate of cloud lowering based on satellite data is shown by the dashed line, and an estimated lowering of the inversion base determined from the radiosonde data is shown with the dotted line. Buoy locations are indicated along the top horizontal axis.

lowers to the surface and forms fog and this fog lifts to form stratus mainly due to the interplay between cooling from the cloud top and warming from the entrained air above the inversion and the surface heat flux. The same test run with stronger subsidence led to strengthening of the inversion and a reduction in heating from the entrained air. In that case, the entire fog layer is slightly cooler and fog remains without occasionally lifting into the cloud layer.

In addition to the above variations, we also combined some of the critical elements for fog formation and performed a test with weak inversion (5 K), low initial cloud top (300 m), and strong subsidence corresponding to divergence of 4×10^{-5} s^{-1}. In this case, the cloud lowered to the surface approximately 20 h into the simulation. Thus, in some cases, strong subsidence imposed on the low-level cloud can overcome the initially weak inversion and fog can form more rapidly and persist for extended periods.

We also investigated how the range of moisture conditions above the inversion alters the evolution of fog. To this end, we have considered one case with dry air above the inversion (initial mixing ratio of water vapor of 1 g kg^{-1}) and another case with moist air above the inversion (initial mixing ratio of water vapor of 5 g kg^{-1}). In the ''dry'' case, the cloud-top longwave cooling was greater than in the ''moist'' case and produced slightly more liquid water prior to fog formation (Fig. 15). After fog formation, there was more liquid water in the ''wet'' case due to entrained moisture.

4. Summary and conclusions

Fog was observed over a limited region of the southern California coast near Point Conception in mid-April 1999. Examination of data from instrumented offshore buoys clearly indicated that near-surface air temperature gradually decreased while the dewpoint temperature

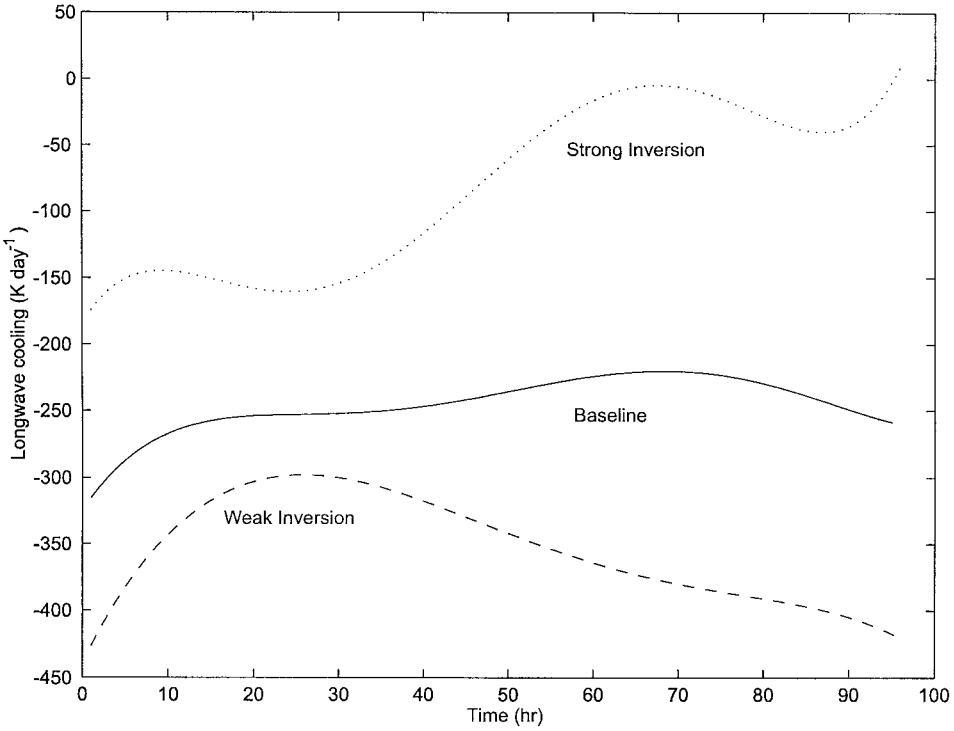

FIG. 13. Time series of the maximum longwave cooling at the cloud/fog top for the baseline simulation (solid line), weak inversion case (dashed line), and strong inversion case (dotted line).

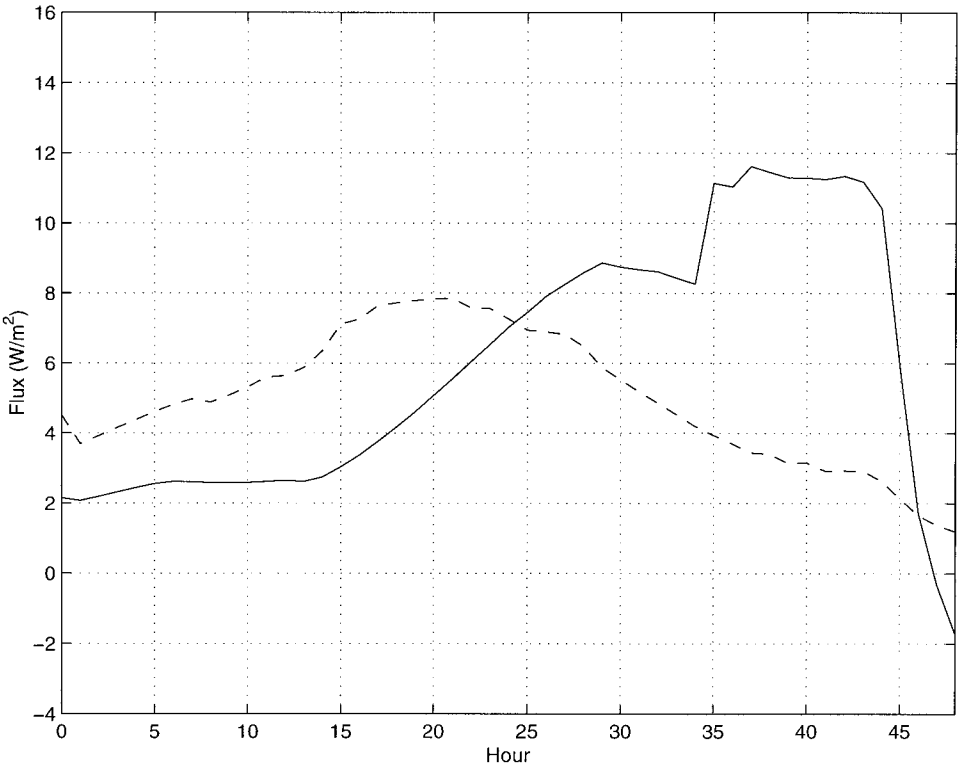

FIG. 14. Time series of the simulated surface sensible heat flux (solid line) and latent heat flux (dashed line) for the strong inversion case.

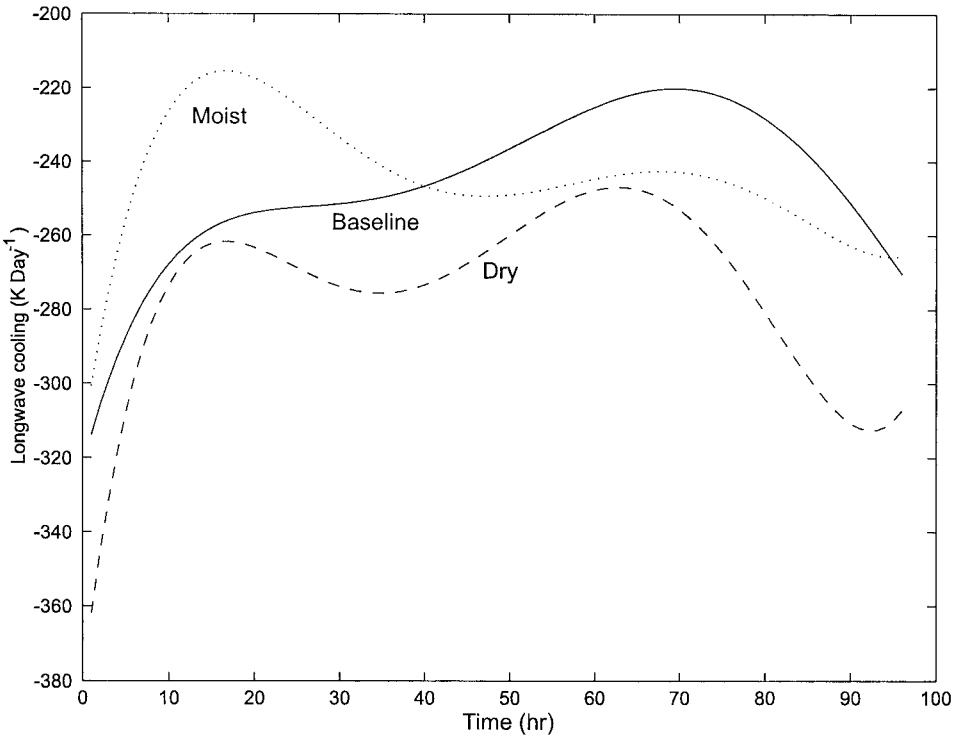

FIG. 15. Time series of the maximum longwave cooling at the cloud/fog top for the baseline simulation (solid line), and cases with dry (dashed line) and moist (dotted line) air above the inversion.

gradually increased. These monotonic changes took place during a period of 24–37 h and led to saturation and fog. From this Eulerian perspective, cooling was difficult to explain since the sea surface was warmer than the air. Furthermore, persistent along-shore winds from the northwest precluded cooling from a land breeze.

The steadiness of these offshore winds for a period of several days led us to view the event from a Lagrangian perspective. We found that the marine layer air associated with fog at Point Conception came from waters offshore of northern California. The journey from the northern waters to Point Conception took 2 days, and satellite observations indicate that the marine layer in this area was mainly capped by stratus cloud throughout the period. Sea surface temperature gradually increased along the trajectory, and an analysis of upper-air observations indicates that a pronounced subsiding northeasterly flow streamed out over the marine layer.

With the synthesis of observations as backdrop, a one-dimensional, second-order turbulence-closure, boundary layer model was used to simulate processes that were unobservable and to test the hypothesis that cloud-top cooling and subsidence were paramount to fog formation. The model was executed in the Lagrangian framework with imposed subsidence and modeled SST variation along the path. The simulation results allowed us to interpret the interplay between large-scale forcing (subsidence and SST) and boundary layer processes that lead to fog formation. The following is a summary of the physical processes germane to the formation of fog:

- Radiative cooling at the cloud top is the primary mechanism for cooling and mixing the marine layer.
- In contrast to previous studies that investigated fog as a result of the cloud base lowering (thickening) in a Eulerian framework, the primary mechanism for fog formation in this study is subsidence-forced lowering of the entire cloud layer along the Lagrangian trajectory. This proposed mechanism has been simulated by the model and has been verified by the observations.
- A warmer ocean leads to an increase in sensible and latent heat fluxes at the air–sea interface which, in turn, heats and moistens the low-level air and also leads to the generation of turbulence; this effect appears to be of secondary importance compared to cloud-top cooling and subsidence.
- It appears that there is an optimum inversion strength conducive to fog formation. The weak inversion induced stronger cloud-top longwave cooling and more liquid water was produced, but fog formed at a later time. The strong inversion led to fog of limited duration and promoted fog dissipation.

- Moisture content of the air above the inversion alters cloud-top longwave cooling and therefore influences the formation and evolution of fog.
- The drop in near-surface air temperature associated with fog formation is counteracted by warming due to the increased ocean–air temperature difference.

Model results were compared to data from buoys, coastal upper-air stations, and a weather satellite at various points along the Lagrangian trajectory. These comparisons generally confirmed the modeled evolution of 1) the temperature–dewpoint temperature trend near the air–sea interface, 2) the descent rate of the stratus cloud top, and 3) the timing of fog onset.

In cool season episodes associated with transitory weather systems, knowledge of the evolution of the marine layer during a period of several days appears crucial. Accurate assessment of this evolution depends on knowledge of the large-scale wind fields, including both vertical and horizontal components. Our results also indicate that success in fog forecasting depends on the model's ability to resolve details of the vertical distribution of radiative fluxes and turbulence within both the cloud and subcloud layers. Without doubt, understanding and predicting coastal fog episodes demands that the cloud-covered turbulent boundary layer processes be viewed in the context of larger-scale synoptic circulation.

Acknowledgments. Two of the authors acknowledge support from the Office of Naval Research: Darko Koračin from the Department of Defense Office of Naval Research: Marine Meteorology and Atmospheric Effects, Grants N00014-96-1-0980, N00014-96-1-1235, and N00014-00-1-0524; and William T. Thompson from Program Element 0601153N. The authors are especially grateful for extended discussions with Dr. Dale Leipper [Desert Research Institute (DRI)]. We credit Mr. Gary Wade, Dr. Fred Wu, and Dr. Robert Rabin of the Space Science and Engineering Center, University of Wisconsin—Madison, Madison, Wisconsin, for satellite products, and Mr. Jim Ashby of DRI for helping us obtain synoptic data. Thanks are due to Ms. Joan O'Bannon of the National Severe Storms Laboratory for graphics support, Mr. Travis McCord and Mr. Domagoj Podnar of DRI for help in the technical preparation of the manuscript, and Mr. Roger Kreidberg of DRI for editorial assistance.

APPENDIX

Details of the Model Algorithm

Prognostic equations for mean variables in a one-dimensional, hydrostatic, incompressible atmosphere with neglected viscous terms are given by

$$\frac{DU}{Dt} - fV = -\frac{1}{\langle\rho\rangle}\frac{\partial P}{\partial x} + \frac{\partial}{\partial z}\left(K_m\frac{\partial U}{\partial z}\right) \quad \text{(A1)}$$

$$\frac{DV}{Dt} - fU = -\frac{1}{\langle\rho\rangle}\frac{\partial P}{\partial y} + \frac{\partial}{\partial z}\left(K_m\frac{\partial V}{\partial z}\right) \quad \text{(A2)}$$

$$\frac{D\theta_l}{dt} = \frac{\partial}{\partial z}\left(K_h\frac{\partial \theta_l}{\partial z}\right) + \sigma_r \quad \text{(A3)}$$

$$\frac{Dq_t}{Dt} = \frac{\partial}{\partial z}\left(K_h\frac{\partial q_t}{\partial z}\right) \quad \text{(A4)}$$

and the turbulence kinetic energy equation is given by

$$\frac{1}{2}\frac{Dq^2}{Dt} = \frac{\partial}{\partial z}\frac{1}{2}\left(qlS_q\frac{\partial q^2}{\partial z}\right) - \overline{u'w'}\frac{\partial U}{\partial z} - \overline{v'w'}\frac{\partial V}{\partial z} + \beta g\overline{w'\theta'_v} + \frac{q^3}{l_1}, \quad \text{(A5)}$$

where U and V are the horizontal wind speed components. The Coriolis parameter is denoted by f. The potential temperature, liquid water potential temperature, equivalent potential temperature, and virtual potential temperature are denoted by θ, θ_l (Betts 1973), θ_e, and θ_v, respectively. The net radiative heating rate is represented by σ_r; q_t, q_v, and q_l are the total water, water vapor, and liquid water mixing ratios, respectively; θ_e is derived from the conservative variables θ_l and q_t, and θ_v is derived from θ, q_v, and q_l. The primed variables denote variances. The stability function is given by S_q (Yamada 1978); β is the thermal expansion coefficient ($=1/\langle\theta\rangle$) where $\langle\ \rangle$ represents a horizontal average, g the acceleration due to gravity, $\overline{w'\theta'}_v$ the kinematic form of buoyancy flux, $\overline{u'w'}$ and $\overline{v'w'}$ are the components of the kinematic form of momentum flux, P is the air pressure, and ρ the air density. The eddy coefficients for turbulent momentum and heat transfer are given by K_m and K_h, respectively. The pressure distribution is calculated from the hydrostatic equation and the vertical wind speed component from the continuity equation. Second-order moments are calculated from the diagnostic expressions [see Yamada (1978) for a complete discussion]. The eddy coefficient for momentum is related to the turbulence kinetic energy (TKE) by the eddy viscosity formula

$$K_m = l[c(q^2/2)]^{0.5}, \quad \text{(A6)}$$

where $q^2/2$ is the TKE and c is a constant equal to 0.2 (Yamada 1983). The mixing length is denoted by l and, following Yamada and Mellor (1979), l_1 is given by 16.6 l.

The surface roughness is calculated according to Charnock (1955):

$$z_0 = 0.016u_*^2/g, \quad \text{(A7)}$$

where u_* is the friction velocity, and the constant 0.016

is obtained from Wu (1969). Similarly z_{0t} is obtained according to Sheppard (1958):

$$z_{0t} = \alpha/ku_*, \tag{A8}$$

and z_{0w} is obtained from

$$z_{0w} = \eta/ku_*, \tag{A9}$$

where k is von Kármán's constant (=0.4) and α and η are the molecular diffusivities for heat and water vapor, respectively. The surface boundary conditions for wind, θ_l and q_t, are the same as those in Yamada and Mellor (1979), that is,

$$(U_1, V_1) = (U_2, V_2)\ \ln(z_1/z_0)/\ln(z_2/z_0) \tag{A10}$$

$$\theta_{l1} = \theta_{l2}\{\ln(z_1/z_{0t})/\ln(z_2/z_{0t})\} + \theta_{l0}\{1 - \ln(z_1/z_{0t})/\ln(z_2/z_{0t})\} \tag{A11}$$

$$q_{l1} = q_{l2}\{\ln(z_1/z_{0q})/\ln(z_2/z_{0q})\} + q_{t0}\{1 - \ln(z_1/z_{0q})/\ln(z_2/z_{0q})\}, \tag{A12}$$

where subscript 0 indicates a surface value and subscripts 1 and 2 indicate the first and second levels from the surface, respectively.

To calculate the turbulent fluxes near the surface, we use the Monin–Obukhov similarity theory, which relates the fluxes to the vertical gradients in the surface layer:

$$\partial U/\partial z = (u_*/kz)\phi_m(z/L), \tag{A13}$$

$$\partial\theta_l/\partial z = (\theta_*/kz)\phi_h(z/L), \tag{A14}$$

$$\partial q_t/\partial z = (q_*/kz)\phi_h(z/L), \tag{A15}$$

where L is the Obukhov length,

$$L = -(u_*^3/k)/[g\overline{\beta(w'\theta_v')}_0], \tag{A16}$$

and $\theta_* = H/\rho c_p u_*$ and $Q_* = E/\rho u_*$ are the temperature and water vapor scales, respectively. Here H and E are the fluxes of heat and moisture at the surface. The functions φ_m and φ_h are obtained from Businger et al. (1971).

We use a simple diagnostic expression for the mixing length (Blackadar 1962):

$$l = k(z + z_0)/[1 + k(z + z_0)/A], \tag{A17}$$

where A is given by

$$A = aV_g/f, \tag{A18}$$

and a is a constant of proportionality and V_g is the geostrophic wind. In order to allow entrainment and growth of the boundary layer, we specify small mixing length above the inversion (2 m).

Mellor (1977) and Sommeria and Deardorff (1977) developed a cloud parameterization based on a Gaussian probability distribution of q_v and θ_l within a given horizontal plane in a one-dimensional model. A modified Gaussian distribution of cloud liquid water was obtained by Yamada and Mellor (1979). The liquid water content is given by

$$q_l = 2\sigma_s(RQ_l + (2\pi)^{-2}\exp(-Q_l^2/2)), \tag{A19}$$

where

$$\sigma_s^2 = \frac{1}{4}\left(a_l^2\overline{q_v'^2} - 2a_lb_l\overline{q_v'\theta_l'} + b_l^2\overline{\theta_l'^2}\right) \tag{A20}$$

$$Q_l = a_l(q_v - q_s)/(2\sigma_s), \tag{A21}$$

and q_s is the saturation mixing ratio and R is the cloud volume given by

$$R = \frac{1}{2}[1 + \mathrm{erf}(Q_l/\sqrt{2})], \tag{A22}$$

where $\mathrm{erf}(x) = (2/\pi)\int_0^x \exp(-y^2)\,dy$. The parameters a_l and b_l are given by

$$a_l = [1 + q_s(L/c_p)]^{-1} \quad \text{and} \tag{A23}$$

$$b_l = a_l(T/\theta)q_s, \tag{A24}$$

where L is the latent heat of evaporation, c_p the specific heat at constant pressure, and T the air temperature. A complete description of this derivation can be found in Yamada and Mellor (1979).

Both shortwave and longwave radiative heat transfer are included in the model. Divergence of the net longwave radiative flux is calculated according to Sasamori (1968). The upper boundary condition at the model domain top for the calculation of the longwave radiative flux is determined by calculating the downward flux through 10 additional levels extending 7400 m above the model domain top. Constant linear profiles of temperature and humidity were assumed in these layers throughout the simulation and the downward longwave flux at the top of the extended domain is determined from Sasamori (1968) and Yamada (1978). The distribution of shortwave heating within a cloud follows the approach of Hanson and Derr (1987). The upper boundary condition at the model domain top for the calculation of the shortwave radiative fluxes was determined from the solar constant, zenith angle, and the pressure path assuming clear-sky conditions and following Yamada (1978).

REFERENCES

Anderson, J. B., 1931: Observations from airplanes of cloud and fog conditions along the southern California coast. *Mon. Wea. Rev.*, **59,** 264–270.

Batchelor, G., 1996: *The Life and Legacy of G. I. Taylor*. Cambridge University Press, 285 pp.

Betts, A. K., 1973: Non-precipitating cumulus convection and its parameterization. *Quart. J. Roy. Meteor. Soc.*, **99,** 178–179.

Blackadar, A. K., 1962: The vertical distribution of wind and turbulent exchange in neutral atmosphere. *J. Geophys. Res.*, **67,** 3095–3102.

Breaker, L., L. Burroughs, and D. Gilhousen, 1998: Preliminary results from long-term measurements of atmospheric moisture in the marine boundary layer in the Gulf of Mexico. *J. Atmos. Oceanic Technol.*, **15,** 661–676.

British Meteorological Office, 1978: *Meteorology for Mariners.* 3d ed. Her Majesty's Stationery Office, 275 pp.

Businger, J. A., J. C. Wyngaard, Y. Izumi, and E. F. Bradley, 1971: Flux-profile relationships in the atmospheric surface layer. *J. Atmos. Sci.,* **28,** 181–189.

Charnock, H., 1955: Wind stress on a water surface. *Quart. J. Roy. Meteor. Soc.,* **81,** 639–640.

Dorman, C. E., L. Armi, J. M. Bane, and D. P. Rogers, 1998: Sea surface mixed layer during the 10–11 June 1994 California coastally trapped event. *Mon. Wea. Rev.,* **126,** 600–619.

Duynkerke, P. G., 1991: Radiation fog: A comparison of model simulation with detailed observations. *Mon. Wea. Rev.,* **119,** 324–341.

——, 1999: Turbulence, radiation and fog in Dutch stable boundary layers. *Bound.-Layer Meteor.,* **90,** 447–477.

Filonczuk, M. K., D. R. Cayan, and L. G. Riddle, 1995: Variability of marine fog along the California coast. Scripps Institution of Oceanography Rep. 95-2, 102 pp. [Available from Scripps Institution of Oceanography, La Jolla, CA, 92093-0224.]

Hanson, H. P., and V. E. Derr, 1987: Parameterization of radiative flux profiles within layer clouds. *J. Climate Appl. Meteor.,* **26,** 1511–1521.

Kondo, J., 1975: Air–sea bulk transfer coefficients in diabatic conditions. *Bound.-Layer Meteor.,* **9,** 91–112.

Koračin, D., 1989: Numerical simulations of the cloud-capped marine boundary layer. Ph.D. dissertation, University of Nevada, Reno, 151 pp.

——, and D. P. Rogers, 1990: Numerical simulations of the response of the marine atmosphere to ocean forcing. *J. Atmos. Sci.,* **47,** 592–611.

Leipper, D. F., 1948: Fog development at San Diego, California. *J. Mar. Res.,* **7,** 337–346.

——, 1994: Fog on the United States west coast: A review. *Bull. Amer. Meteor. Soc.,* **75,** 229–240.

——, and D. Koračin, 1998: Hot spells and their role in forecasting weather events on the U.S. west coast. Preprints, *Second Conf. on Coastal Atmospheric and Oceanic Prediction and Processes,* Phoenix, AZ, Amer. Meteor. Soc., 127–132.

Mack, E. J., U. Katz, C. Rogers, and R. Pilié, 1974: The microstructure of California coastal stratus and fog at sea. Calspan Corp. Rep. CJ-5405-M-1, 74 pp. [Available from Desert Research Institute, 2215 Raggio Parkway, Reno, NV 89512].

Mellor, G. L., 1977: The Gaussian cloud model relations. *J. Atmos. Sci.,* **34,** 356–358.

Neiburger, M., D. S. Johnson, and C. W. Chien, 1961: *The Inversion over the Eastern North Pacific Ocean.* Vol. 1, *Studies of the Structure of the Atmosphere over the Eastern Pacific in Summer,* University of California Press, 58 pp.

Nicholls, S., 1984: The dynamics of stratocumulus: Aircraft observations and comparison with a mixed layer model. *Quart. J. Roy. Meteor. Soc.,* **110,** 783–820.

Oliver, D., W. Lewellen, and G. Williamson, 1978: The interaction between turbulent and radiative transport in the development of fog and low-level stratus. *J. Atmos. Sci.,* **35,** 301–316.

Petterssen, S., 1938: On the causes and the forecasting of the California fog. *Bull. Amer. Meteor. Soc.,* **19,** 49–55.

Pilié, R. J., E. J. Mack, C. W. Rogers, U. Katz, and W. C. Kocmond, 1979: The formation of marine fog and the development of fog-stratus systems along the California coast. *J. Appl. Meteor.,* **18,** 1275–1286.

Rogers, D. P., and D. Koračin, 1992: Radiative transfer and turbulence in the cloud-topped marine atmospheric boundary layer. *J. Atmos. Sci.,* **49,** 1473–1486.

Sasamori, T., 1968: The radiative cooling calculation for application to general circulation experiment. *J. Appl. Meteor.,* **7,** 721–729.

Saucier, W. J., 1955: *Principles of Meteorological Analysis.* University of Chicago Press, 438 pp.

Sheppard, P. A., 1958: Transfer across the earth's surface and through the air above. *Quart. J. Roy. Meteor. Soc.,* **84,** 215–224.

Smith, W. S., and C.-Y. J. Kao, 1996: Numerical simulations of observed Arctic stratus clouds using a second-order turbulence closure model. *J. Appl. Meteor.,* **35,** 47–59.

Sommeria, G., and J. W. Deardorff, 1977: Subgrid-scale condensation in models of precipitating clouds. *J. Atmos. Sci.,* **34,** 344–355.

Stage, S. A., and J. A. Businger, 1981a: A model for entrainment into a cloud-topped marine boundary layer. Part I: Model description and application to a cold-air outbreak episode. *J. Atmos. Sci.,* **38,** 2213–2229.

——, and ——, 1981b: A model for entrainment into a cloud-topped marine boundary layer. Part II: Discussion of model behavior and comparison with other models. *J. Atmos. Sci.,* **38,** 2230–2242.

Taylor, G. I., 1917: The formation of fog and mist. *Quart. J. Roy. Meteor. Soc.,* **43,** 241–268.

Telford, J., and S. K. Chai, 1984: Inversions and fog, stratus and cumulus formation in warm air over cooler water. *Bound.-Layer Meteor.,* **29,** 109–137.

Tjernström, M., and D. Koračin, 1995: Modeling the impact of marine stratocumulus on boundary layer structure. *J. Atmos. Sci.,* **52,** 863–878.

Wu, J., 1969: Wind stress and surface roughness at air–water interface. *J. Geophys. Res.,* **74,** 444–455.

Yamada, T., 1978: A three-dimensional, second-order closure numerical model of mesoscale circulation in the lower atmosphere. Topical Rep. ANL/RER-78-1, Radiological and Environmental Research Division, Argonne National Laboratory, Argonne, IL, 67 pp.

——, 1983: Simulations of nocturnal drainage flows by a q^2l turbulence closure model. *J. Atmos. Sci.,* **40,** 91–106.

——, and G. L. Mellor, 1979: A numerical simulation of the BOMEX data using a turbulence closure model coupled with ensemble cloud relations. *Quart. J. Roy. Meteor. Soc.,* **105,** 915–944.